Flow separation in airfoils with rough leading-edges

Vishal Kumar *
Queen's University, Kingston, Ontario, K7L 2V9, Canada

Arnau Miró [ID] † and Oriol Lehmkuhl [ID] ‡
Barcelona Supercomputing Centre, Barcelona, 08034, Spain

Ugo Piomelli [ID] §
Queen's University, Kingston, Ontario, K7L 2V9, Canada

In this study we consider the flow over airfoils with leading-edge roughness, designed to mimic the ice depositions that may occur on an aircraft in flight. The focus of this investigation is the effect of the angle-of-attack on the mean-flow three-dimensionality. In previous work [Kumar *et al.* (*J. Turb.*, vol. 22(11), 2021, p. 735-760)] we found stationary spanwise inhomogeneities, in the form of alternating regions of fast and slow-moving fluid, which were termed "flow channels". In the present study we investigate further this phenomenon. We observe the formation of hairpin vortices downstream of the roughness elements, that eventually merge; this causes the formation of wider channels that remain coherent and affect the trailing-edge separation. With increasing angle of attack the intensity of flow-channelling can increase or decrease depending on the topology of the leading-edge roughness. Its effect on the trailing-edge separation remains, however, significant. The mean-separation line is highly distorted, and the separation length can vary by up to 30% of the chord length along the span.

---

*Ph.D. candidate, Department of Mechanical & Materials Engineering, 130 Stuart St.
†Recognized Researcher, CASE - Large-scale Computational Fluid Dynamics, Plaça d'Eusebi Güell, 1-3.
‡Team Leader, CASE - Large-scale Computational Fluid Dynamics, Plaça d'Eusebi Güell, 1-3.
§Professor, Department of Mechanical & Materials Engineering, 130 Stuart St., Associate Fellow AIAA.

I. Nomenclature

x, y, z	=	streamwise, vertical and spanwise directions	c_p, c_f	=	coefficient of pressure and friction
t, n	=	tangential and normal directions in xy-plane	$\mathcal{L}, \mathcal{D}$	=	lift and drag forces per unit span
s, d	=	tangential and normal distance from airfoil	c_l, c_d	=	lift and drag coefficient
u, v, w	=	streamwise, vertical and spanwise fluid velocity	τ_w	=	wall shear stress
p	=	fluid pressure	u_τ	=	friction velocity
$\widetilde{\cdot}$	=	filtering operator	u^+	=	viscous scaled (u)
τ_{ij}	=	sub-filter scale (SFS) stresses	N_{dof}	=	number of degrees of freedom
$\bar{\cdot}$	=	time averaging operator	N_z	=	number of spanwise planes
$\langle \cdot \rangle$	=	span averaging operator	x_{sep}	=	trailing edge separation location
ν	=	kinematic fluid viscosity	δ_{95}	=	95% boundary layer thickness
c	=	airfoil chord	ΔU_t	=	maximum spanwise difference in U_t
U_o	=	reference inflow velocity	$\boldsymbol{\Omega}$	=	angular rotation rate tensor
Re	=	chord based Reynolds number	$\mathbf{S}$	=	strain-rate tensor
AoA, α	=	angle of attack	$\mathcal{K}$	=	turbulent kinetic energy
h	=	roughness height			
β	=	Rotta-Clauser pressure-gradient parameter			
Q	=	second-invariant of the velocity-gradient tensor			

II. Introduction

For nearly a century aeronautical designers have tried to maintain laminar flow on aircraft wings. If transition to turbulence can be prevented, much lower drag can be achieved, lowering the fuel consumption and increasing the range of aircraft. Early attempts to design laminar-flow airfoils, in which transition was delayed by tailoring the airfoil shape to obtain a favourable pressure gradient over a large part of the airfoil, were only partially successful [1]. While wind-tunnel tests showed a marked decrease in the drag coefficient over a range (usually relatively small) of angles of attack, in practice imperfections due to manufacturing, fouling of the surface, or ice accretion resulted in the transition to turbulence much earlier than observed in the laboratory. Recently, renewed effort has been made to maintain laminar flow on the engines nacelles. In Natural Laminar Flow (NLF) nacelles laminar flow can be maintained over 10-15% of the nacelle length, resulting in drag reduction that can be as high as 1-2% of the total drag.

Surface imperfections, however, can disrupt the flow and cause early transition to turbulence. They can be due to the manufacturing process (gaps between metal plates, rivets etc.), or to natural phenomena such as ice formation. Ice

depositions, in particular, have very negative effects, since they affect the lift as well as the drag. Thus, much research has been carried out in this area, focused on determining the ice shapes encountered in practice, and the effects of these ice-shapes on the flow field. A complete review of icing research can be found in papers by Gent *et al.* [2] and Cebeci and Kafyeke [3]. A discussion of the research relevant to the present investigation can also be found in the recent paper by Kumar *et al.* [4]; here we summarize the main results of these studies.

Previous research into ice-accretion through experiments and numerical simulations identified a variety of ice shapes and associated aerodynamic effects. One of the four major categories of ice-shapes, "ice-roughness", occurs in the initial phase of the accretion process, when the accumulations are small. The initial geometry is three-dimensional, whereby water content in clouds freeze on the body upon impact and act as isolated roughness elements. With time, however, the roughness grows and the topology becomes a quasi-two-dimensional spanwise ridge.

The reviews of experimental works involving iced airfoils by Lynch & Khodadoust [5] and Bragg *et al.* [6] discuss mainly the degradation of airfoil performance. Although these studies mention a wide range of aerodynamic effects associated with the presence of ice-roughness on airfoils, a detailed analysis of flow-physics was never reported. In a recent review of previous numerical studies of iced-airfoils, Stebbins *et al.* [7] found no eddy-resolving study of ice roughness geometry to have ever been conducted.

Kumar *et al.* [4] performed large-eddy-simulations (LES) of flow over smooth and rough NACA4412 airfoils at Reynolds number $Re = U_o c / \nu = 200,000$ (where c is the chord length, U_o the free-stream velocity, and ν the kinematic viscosity) and angle of attack $\alpha = 5^o$. To the best of our knowledge, this was the first eddy-resolving simulation of the flow over large, spatially heterogeneous leading-edge obstacles mimicking aircraft icing on an airfoil. They analyzed the effect of variations of the roughness shape for geometries mimicking accretion of the ice-roughness kind. The primary effect of the roughness three-dimensionality is to create a stationary spanwise heterogeneity of the flow statistics (a phenomenon that they called "flow-channelling"), whereby fluid at different spanwise location near the leading edge move at different velocities. The high- and low-speed channels had widths of the order of the roughness size. Kumar *et al.* [4] also found that, while the regions of fast-moving fluid (which occur behind roughness elements and were called "peak regions") resemble an accelerating boundary layer, the regions of slower fluid (which are found between the roughness peaks, and were termed "valley regions") have characteristics that are similar to a decelerating boundary-layer. Additionally, the flow channelling was shown to be sensitive to the sign of the pressure gradient, as they remained more coherent on the pressure side than on the suction side.

Similar phenomena had been observed in studies of boundary-layer transition over distributed roughness [8–10], and of turbulent boundary layer flow over random roughness [11–14]. In the former cases, the ensuing heterogeneities were called either "streaks" or "merged low-speed blobs" (MLSs), in the latter "low-" and "high-momentum pathways" (LMP, HMP). Compared to the the LMPs and HMPs present in turbulent boundary-layer flow, however, the scale of the channelling phenomenon described in [4] is much larger. Note also that most of these studies are performed on flat-plate

boundary layer configurations with zero-or-moderate pressure gradients, where flow separation does not occur [4].

Studying the effect of the flow channels on separation is particularly important. Flow separation severely affects the aerodynamic characteristics of an airfoil, and its accurate prediction is critical for the design of the wing. However, the prediction of flow separation using classical Reynolds-Averaged Navier-Stokes (RANS) models is a longstanding bottleneck in the field of turbulence modelling. Spalart [15] noted that both the accurate location of the separation point and the momentum transfer after separation remain a major challenge for these models. In an effort to quantify the behaviour of different RANS frameworks, [16] studied the behaviour of a linear eddy viscosity and a Reynolds stress model for flow over 2D bump. They found that none of these models were able to predict flow separation at the tested configuration. Notwithstanding their inherent shortcomings, RANS models remain the workhorses of applied CFD [17] due mainly to their very low computational cost. Most of the studies over iced airfoils depend on these models and, hence, there is a need to refine the associated error limits.

With these consideration in mind, we extended the study by Kumar *et al.* [4] by carrying out large-eddy simulations (LES) of the same airfoil, at higher angles-of-attack. Our objective is to investigate the dynamics that cause the generation of this channels, and quantify their effect on the separation. In the following we will first formulate the problem, in terms of numerical method, physical model and geometric configuration. Then we will validate the simulations, and present the results. Finally, comments and recommendations for future work will conclude the paper.

III. Problem formulation and methodology

A. Governing equations

The flow over a NACA 4412 airfoil at $Re = 200,000$ (based on free-stream velocity U_o and chord length c) was studied using Wall-Resolved Large-Eddy Simulations (WRLES). Three angles-of-attack, $\alpha = 5^o$, 10° and 15° were considered. The filtered Navier-Stokes equations for incompressible flow were solved:

$$\frac{\partial \tilde{u}_i}{\partial x_i} = 0. \tag{1}$$

$$\frac{\partial \tilde{u}_i}{\partial t} + \frac{\partial}{\partial x_j}\left(\tilde{u}_i\tilde{u}_j\right) = -\frac{1}{\rho}\frac{\partial \tilde{p}}{\partial x_i} - \frac{\partial \tau_{ij}}{\partial x_j} + \nu\frac{\partial^2 \tilde{u}_i}{\partial x_j \partial x_j}. \tag{2}$$

where $\tau_{ij} = \widetilde{u_iu_j} - \tilde{u}_i\tilde{u}_j$ are the unresolved Sub-Filter Scale (SFS) stresses, x, y, z (or x_1, x_2, x_3) are the streamwise, vertical and spanwise directions, respectively. The corresponding filtered instantaneous pressure and velocity fields are $\tilde{p}$ and $\tilde{u}$, $\tilde{v}$, $\tilde{w}$ (or $\tilde{u}_i$). We will also be using subscripts t and n to indicate the velocity components tangential and normal to the airfoil surface in the $xy-$plane. In the following, the tilde will be dropped; u_i and p will be implicitly assumed to be filtered quantities.

The unresolved, subfilter-scale, stresses are modelled using either the ILSA model [18] (for $\alpha = 5^o$ cases), in its
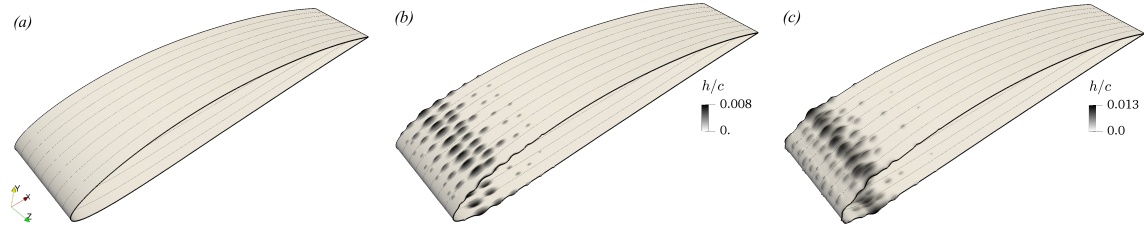
Fig. 1 Airfoil geometries: *(a)* **Smooth Leading Edge (SLE);** *(b)* **Rough Leading Edge 1 (RLE1);** *(c)* **Rough Leading Edge 2 (RLE2). The roughness elements are coloured based on their height** h**, relative to the surface of the unmodified airfoil.**

local formulation [19] or the WALE model of Nicoud and Ducros [20], for higher angles-of-attack. This change was motivated by the lower computational cost of the WALE model. The model parameter for ILSA, s_τ, which measures the SFS contribution to the dissipation, is set to 0.1 based on the recommendation of Lehmkuhl *et al.* [21] for prismatic elements. The model parameter for WALE model is also set to 0.1. Both the models have been validated against each other for one of the smooth cases at $\alpha = 5^o$ and compare very well.

The simulations in this study are performed using Alya, a multi-physics, massively parallelized, unstructured finite-element simulation code developed at Barcelona Supercomputing Center [22, 23]. It has been widely validated in many turbulent-flow configurations: [21, 24–28]. The governing equations (1) and (2) are discretised on a collocated unstructured grid by means of low dissipation second-order schemes using energy, momentum and angular momentum conserving (EMAC) form of the non-linear convective term [29, 30]. The same interpolation scheme for velocity and pressure is used in space. A third-order Runge-Kutta explicit time-discretization is used to advance the solution in time, combined with an eigenvalue-based time-step estimator [31]. A fractional time-step algorithm is used to solve the resulting system of linear equations [30]. The Poisson equation is solved using a Deflated Conjugate Gradient[32]; convergence and stopping criteria are based on the lagged algebraic residual.

B. Airfoil geometries

Three surface geometries (shown in Figure 1) were studied. They are all based on the NACA 4412 airfoil, with various leading-edge modifications. In addition to the unmodified airfoil with a smooth leading-edge (SLE), we considered two Rough Leading-Edge cases (RLE1 and RLE2) with randomly distributed roughness elements.

The RLE1 and RLE2 cases aim to reproduce the ice accretions in the study by McClain *et al.* [33] (see Figure 3 in that paper). The roughness elements were ellipsoids; their height, h, depended on their x location, to have a similar distribution as in [33]. The maximum peak-height, $h_{p,\max}$, was $0.008\,c$ and $0.013\,c$ for the RLE1 and RLE2 cases, respectively. The corresponding mean peak-roughness height, $\overline{h}_p$, was $0.004\,c$ and $0.009\,c$. Since the roughness elements were located close to the leading edge, where the boundary layer is very thin, they extend outside the boundary layer and act as flow obstacles.

Although care was taken for these geometries to resemble those found in the experiments of McClain *et al.* [33], some simplifications were required to maintain grid quality. The spacing between the elements, for instance, is nearly constant (with a small random variation) and their shape is ellipsoidal. The ice deposition, shown by [33], has a more random distribution. By matching the height distribution and length scale of the real ice roughness, however, we retained key elements of a real geometry.

C. Computational domain and boundary conditions

All computations were carried out on a $40c \times 40c \times 0.2c$ C-type domain, with the leading edge placed at the origin. This choice of domain size, particularly the spanwise extent of 20% of chord, is consistent with previous studies in the literature [34–37]. At low Reynolds number finite-size effects may be observed with this domain size at angles of attack beyond stall [38, 39]; the present simulation, however, is carried out at a Reynolds number an order of magnitude higher than in the studies, so that these effects are less significant. The spanwise two-point correlation (TPC) of the velocity near the airfoil surface was computed for $\alpha = 5$ and 10°, and confirmed this conjecture (not shown).

An open-source grid-generation tool, Gmsh [40], was used to generate the mesh. A body-fitted grid with triangular-prism elements was used, and mesh smoothing was employed in all directions to maintain grid quality. Parameters related to the final meshes used are listed in Table 1. There were 25-30 points within the boundary layer, in accordance with the recommendation of Choi & Moin [41]. Triangular prisms have been used previously with Alya, in studies that include turbulent flow over spheres [26, 42], and over airfoils [28, 39, 43]; the results were in consistently good agreement with the reference data. Furthermore, the need to resolve the roughness elements dictates the grid size in the streamwise direction; hexahedral elements, therefore, would not result in the same computational savings realized, for instance, on smooth surfaces, and the quality of the grid near the roughness elements would probably be lower. A sample grid used in this study is shown in Figure 2; a uniform element-size in x is used on the airfoil surface while the grid is stretched in the direction normal to the body.

The boundaries used the following conditions: at the inlet a uniform velocity $(u, v, w) \equiv (U_o \cos \alpha, U_o \sin \alpha, 0)$ was assigned; at the outlet, a pressure-based condition was applied, where the total pressure (p_d) and outlet normal velocity (u_n) are related by $p_d = \frac{1}{2}\rho u_n^2$. No-slip conditions were imposed on the airfoil surface, and the flow was assumed to be periodic in the spanwise direction. Since no disturbances were introduced artificially, the flow transitions naturally from the amplification of small perturbations (due to round-off or truncation error). As will be shown, the presence of leading-edge imperfections plays a critical role in the transition process.

The computational methodology has been thoroughly validated for different flows of this type [21, 28, 34, 44], in terms of both numerical scheme and SFS model. In our previous work we showed that the pressure coefficient in the SLE-5° case matches very well the experimental data of Mallor *et al.* [45]; data for c_d was not reported in this reference. Here we also compare with the lift and drag coefficients from the wind-tunnel experiments (with inlet turbulent intensity
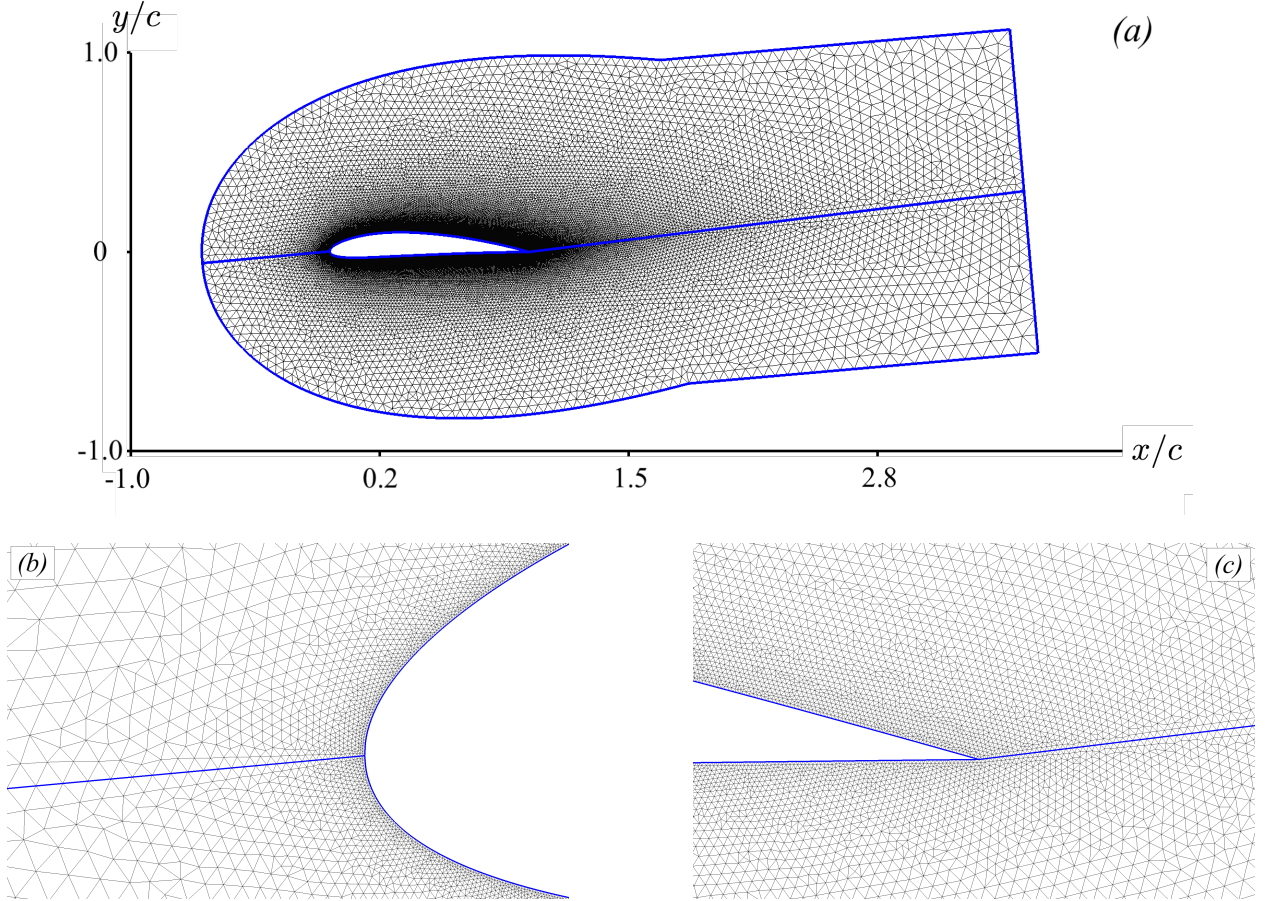
Fig. 2 Sample grid distribution; actual grid densities for different cases are reported in Table 1. *(a)* Grid distribution near the airfoil; *(b)* enlargement of the leading edge, and *(c)* of the trailing edge.

~ 0.25%) of Ostowari *et al.* [46], who used a smooth NACA 4412 airfoil at the three angles of attack that we have used, but for slightly higher value of $Re = 250,000$. The lift coefficient is in good agreement with the data, while the drag prediction is consistently lower than the experiments. Given the difference in Reynolds number, and in the inlet turbulence (our study uses laminar inflow) this is to be expected and will be discussed in detail in the upcoming sections.

IV. Results

A. Grid resolution

Kumar *et al.* [4] performed a grid-convergence study for the 5° angle that showed that the resolution used in their paper (the same as in the present one) is sufficient to capture first-order statistics (with an error of less than 4%). To evaluate whether this grid is sufficient at the higher angles-of-attack as well, we show in Figure 3 the wall-normal and spanwise grid size, in wall units (i.e., normalized by ν/u_τ, where $u_\tau = (\bar{\tau}_w/\rho)^{1/2}$ is the local friction velocity and an overbar denotes a time-averaged quantity) for the three angles of attack and the RLE1 geometry. On the suction side the

Case	N_z	N_y/δ	$h_{max}/\Delta s$	$h_{max}/\Delta n$	$h_{max}/\Delta z$	$N_{dof} \times 10^{-6}$
SLE	145	> 25	-	-	-	28.3
RLE1	145	> 35	40	40	6	28.3
RLE2	145	> 45	65	65	10	28.3

Table 1 **Summary of computational mesh parameters for different cases at $\alpha = 5°$. N_y: number of points in the wall-normal direction; δ: boundary layer thickness; N_z: number of points in the spanwise direction; h_{max}: maximum roughness height; Δs, Δn: grid spacing in wall-parallel and wall-normal directions; N_{dof}: number of degrees of freedom; data for N_y/δ is shown for the turbulent part of the boundary layer.**
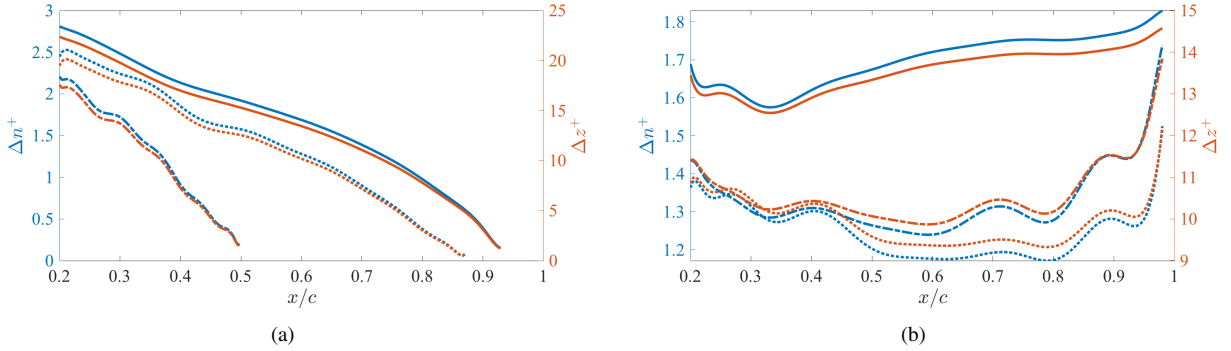

(a)

(b)

Fig. 3 **Distribution of wall-normal and spanwise resolution in plus units for RLE1 case;** *(a)* **suction side;** *(b)* **pressure side; blue lines:** Δn^+; **red lines:** Δz^+; **solid lines:** 5°; **dotted lines:** 10°; **dashed lines:** 15°.

viscous length-scale increases due to the adverse pressure gradient. The grid size in wall units, therefore, also decreases. On the pressure side the favourable pressure gradient causes the flow to tend towards a quasi-laminar state (in fact, at 15°, for the RLE1 case the flow remains laminar on the pressure side). There is an increase in wall stress as the trailing-edge is approached, but the grid spacing remains below that of the 5° case throughout. Since, for the 10° and 15° cases the grid size is lower (in wall units) than that used in the grid-converged 5° case, we conclude that the resolution used is adequate for all cases.

B. Instantaneous flow field

Figures 4 shows iso-surfaces of the second invariant of the velocity-gradient tensor,

$$Q = \frac{1}{2}\left(|\mathbf{\Omega}|^2 - |\mathbf{S}|^2\right)$$
(3)

where $\mathbf{\Omega}$ and $\mathbf{S}$ are the rotation and rate-of-strain tensors.

In the SLE cases (figures 4*(a,b,c)*), the incoming flow remains laminar and separates relatively early. Transition to turbulence occurs in the separated shear-layer. The location of flow separation, marked by solid black arrow
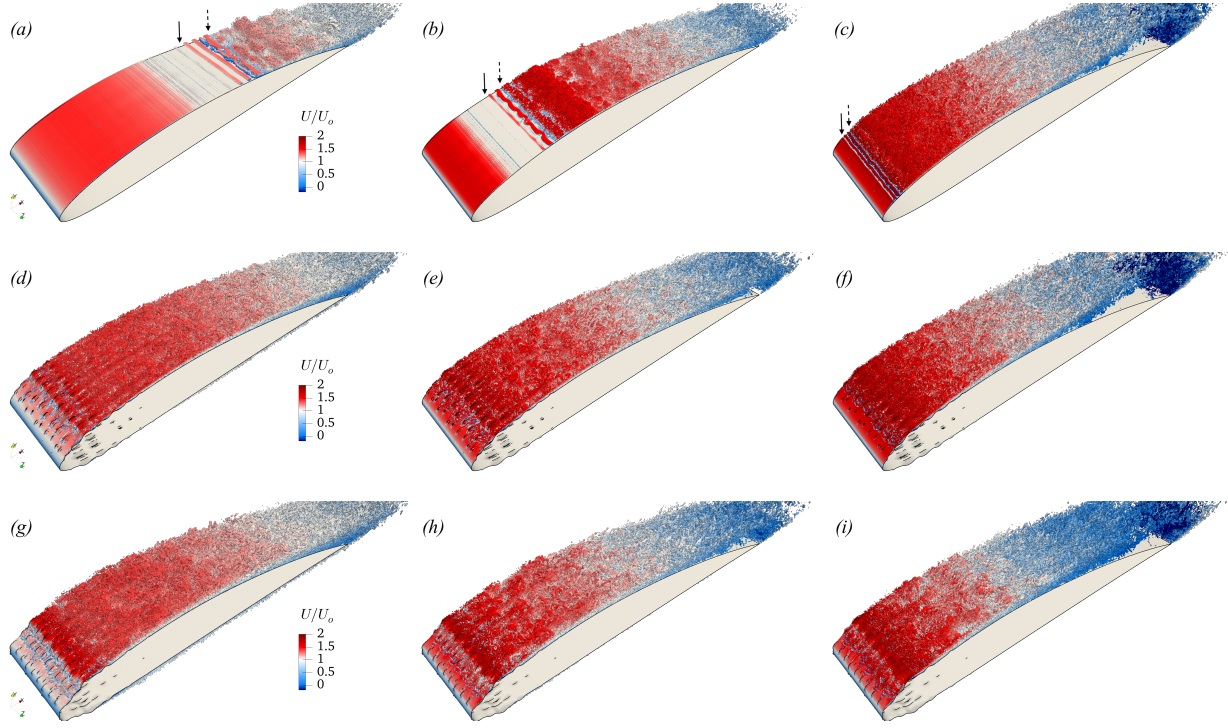
Fig. 4   Iso-surfaces of $Q = 200\,U_{\max}^2/c^2$, where $U_{\max}$ is the maximum averaged streamwise velocity, coloured by the time-averaged streamwise velocity U/U_o for *(a,b,c)* **SLE case;** *(d,e,f)* **RLE1 case;** *(g,h,i)* **RLE2 case;** *(a,d,g)* $\alpha = 5°$; *(b,e,h)* $\alpha = 10°$; *(c,f,i)* $\alpha = 15°$.

in the figure, progressively moves upstream with increasing angle due to increase in the magnitude of the adverse pressure-gradient (APG). The streamwise length over which the flow transitions also shortens as the angle of attack increases. The transition process begins with the generation of spanwise vortices in the separated shear-layer, due to the Kelvin-Helmholtz instability. The spanwise vortices then become three-dimensional, reattach, and break down immediately thereafter (the dashed black arrow marks the appearance of the secondary instability), and finally develop into the typical hairpin structures associated with wall turbulence. Although the turbulent boundary layer for the 5° and 10° cases remains attached, the 15° configuration experiences massive trailing-edge flow separation (Figures 4*(c)*).

Flow transition in the rough cases initiates at the first row of roughness elements. We observe the generation of small-scale structures very close to the roughness patch. As the angle of attack increases to 15°, there is some similarity in flow features between the smooth and the rough cases, particularly for the RLE1 case. Conversely, in the RLE2-15° case there is a stronger three-dimensionality of the structures in the spanwise direction. As will be discussed momentarily, this variation is evident in the statistics as well, affecting the location of trailing-edge separation substantially.

9

Case	$\alpha = 5°$				$\alpha = 10°$				$\alpha = 15°$			
	c_l	c_d	$\%c_{d_p}$	x_{sep}^{avg}	c_l	c_d	$\%c_{d_p}$	x_{sep}^{avg}	c_l	c_d	$\%c_{d_p}$	x_{sep}^{avg}
SLE	0.95	0.018	53	-	1.35	0.029	72	-	1.34	0.076	85	0.58
RLE1	0.82	0.027	52	0.93	1.17	0.042	76	0.86	1.24	0.093	89	0.51
RLE2	0.77	0.034	64	0.94	1.08	0.054	82	0.80	1.16	0.115	92	0.54
Exp.	1.01	0.025	-	-	1.26	0.047	-	-	1.41	0.088	-	-

Table 2   Summary of the lift (c_l) and drag (c_d) coefficients, of the contribution to c_d of the form drag, as a percentage of c_d, and average trailing-edge-separation location (x_{sep}^{avg}). The data of Ostowari *et al.* [46], who conducted experiments on a smooth NACA4412 profile at $Re = 250,000$ is also listed.

C. Aerodynamic coefficients

The lift and drag coefficients are defined as

$$c_l = \frac{2\mathcal{L}}{\rho U_o^2 c} \quad c_d = \frac{2\mathcal{D}}{\rho U_o^2 c}, \tag{4}$$

where $\mathcal{L}$ and $\mathcal{D}$ are the lift and drag forces per unit span. The lift coefficient c_l for the SLE case saturates at $\alpha = 10^o$, while the drag coefficient c_d increases more than two-folds when the angle is increased to 15°. The contribution of form drag increases from 50% at 5° to almost 85% at 15°, reflecting the effect of flow separation. As mentioned earlier, the c_l matches quite well the experiments of Ostowari *et al.* [46]. The c_d, however, is consistently lower than in the experiments, particularly at the lower α. The boundary layer in the present configuration undergoes transition via a laminar separation bubble (LSB) and the observed difference between our cases and Ostowari *et al.* [46] might be related to the sensitivity of LSB to Reynolds number, and to the fact that no perturbations were introduced at the inflow in the simulations while in the experiment the inlet turbulence intensity was 0.25%.

The impact of roughness is to degrade the aerodynamic performance of the airfoil at all the angles-of-attack studied, by reducing the lift and increasing the drag. The differences in lift coefficient between the smooth and rough cases, however, decreases as the angle of attack increases to 15°. As will be discussed momentarily, with increasing α the flow interaction with the leading edge roughness is weaker. This helps boost the peak suction pressure even for the rough cases and, consequently, increases the lift. Owing to its greater roughness height, RLE2 -type roughness (which is 60% higher than for the RLE1 case) causes a much larger drag force; the contribution of pressure drag is also much greater than for RLE1 roughness at all angles considered. Both roughness types cause the flow to separate much earlier at the trailing edge than the baseline smooth cases.

D. Time averaged flow

In our previous study [4], we observed that while the behaviour of RLE1 at $\alpha = 5^o$ was similar to that of the three-dimensional distributed roughness representative of initial ice-accretion dynamics, the RLE2 case behaved more
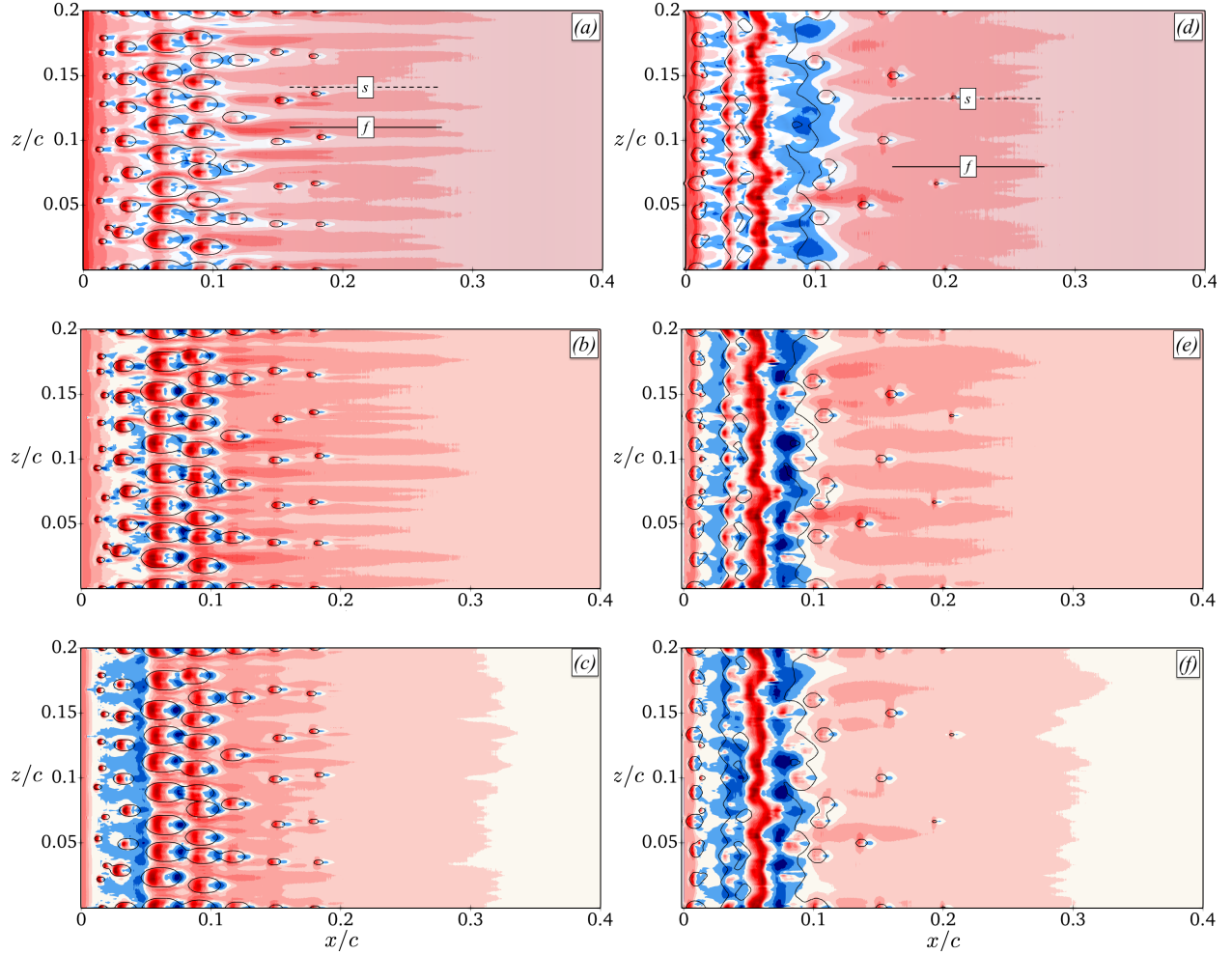
Fig. 5 Time-averaged tangential wall-shear stress ($\overline{\tau}_{w,t}/\rho U_o^2$) in the roughness region on the suction side of the airfoil. *(a,b,c)* RLE1 case; *(d,e,f)* RLE2 case; *(a,d)* $\alpha = 5°$; *(b,e)* $\alpha = 10°$; *(c,f)* $\alpha = 15°$. **Contour levels: blue (-0.01); white (0); red (+0.04). Black contour lines show a roughness level** $h/c = 0.001$; **slow (s) and fast (f) regions have been marked and labelled in** *(a,d)*.

like a spanwise ridge with limited three-dimensionality. We also showed that flow channelling near the leading edge was sensitive to the pressure gradient sign on the airfoil, the channels remaining more coherent on the pressure side because of the FPG. Here, we are focusing on the effect of the channelling on separation and, therefore, we will confine ourselves to the description of the effects of roughness on the the APG boundary layer developing on the suction side of the airfoil.

Figure 5 shows contours of the time-averaged tangential wall-stress, defined as

$$\overline{\tau}_{w,t} = \rho \nu \frac{\partial \overline{u}_t}{\partial n}\bigg|_{d=0} \tag{5}$$

where d is the distance normal to the airfoil, near the roughness region of the airfoil on the suction side, for the two rough geometries. The 3D and mixed 2D/3D topology of roughness is evident in Figure 5*(a,d)*, which shows several

isolated recirculation regions behind the roughness elements for the RLE1-5° case, and a merged one for the RLE2-5° case. As the angle of attack increases, the interaction of the roughness elements with the flow is limited, as the incoming momentum of the attached flow is reduced by the adverse pressure gradient, which starts immediately downstream of the LE; at 5° it happens at about 2 percent of the chord. This can be seen for the RLE1 case (Figures 5(a,b,c)), where the streaky nature of the wall shear-stress distribution is substantially reduced as the angle of attack increases. Further evidence of this effect is for the RLE1-15° case where an APG-induced separation, remarkably similar to that in the SLE-15° case (not shown), is present near the location of smaller elements ($x/c \lessapprox 0.05$). For roughness of RLE2 kind, however, the effect of angle of attack is not straightforward. As the angle of attack is increased from 5° to 10° the wall shear-stress becomes more streaky (Figure 5(d,e)). In the RLE2 case, the roughness elements nearly merge at their base, but their crests are distinct, and form a more 3D array. Since (as in the RLE1 case) the incoming flow interacts mostly with the roughness peaks at high angle of attack the flow channelling is more pronounced. However, further increase of angle to 15° (Figure 5(f)) results in a behaviour similar to that of RLE1 case and flow channelling seems to subside.

The pressure and friction coefficients, c_p and c_f, are defined as:

$$c_p = \frac{P - P_o}{1/2 \rho U_o^2}; \qquad c_f = \frac{\langle \overline{\tau}_{w,t} \rangle}{1/2 \rho U_o^2} \tag{6}$$

where P_o is a freestream pressure (set as zero). They are shown in Figure 6. As expected, for the SLE case, with increasing angle of attack the pressure decreases on the suction side and increases on the pressure side (Figure 6(a)). The x-location of minimum pressure, which marks the change of favourable to adverse pressure gradient zone, does not change very significantly as angle of attack is increased from $10°$ to $15°$. The APG destabilizes the boundary layer, and hastens transition to turbulence. As the angle of attack increases, the APG becomes stronger, and the transition point moves upstream ($x/c = 51\%$, 14%, 4.2% for the three angles; Figure 6(b)). The flow transition appears to be similar for $5°$ and $15°$ angles, where it is due to the amplification of the shear-layer instabilities just after flow separation; the classical markers of such a transition can be seen in Figure 6(b). The length of the separation bubble (L_{lsb}) in the SLE-15° case ($L_{lsb} = 3.6\% \, c$), however, is smaller than for the SLE-5° case ($L_{lsb} = 14\% \, c$), indicating faster transition for the higher angle of attack configuration. The c_f for the SLE-10° case (red line in Figure 6(b)), on the other hand, shows no flow separation in a time-averaged sense, and the transition to turbulence is swifter than in the other two angle of attack cases. As discussed in Section IV.B, although the instantaneous data for the SLE-10° case shows separation, the flow transition at this configuration is highly unsteady (see included animation as supplementary material), such that the transition location periodically oscillates in the streamwise direction. This unsteadiness is consistent with the observations of various studies [39, 47] that report the presence of oscillations of the laminar separated shear layer near the stall angle.

Roughness at the leading edge interacts with the incoming flow and modifies the pressure distribution, when
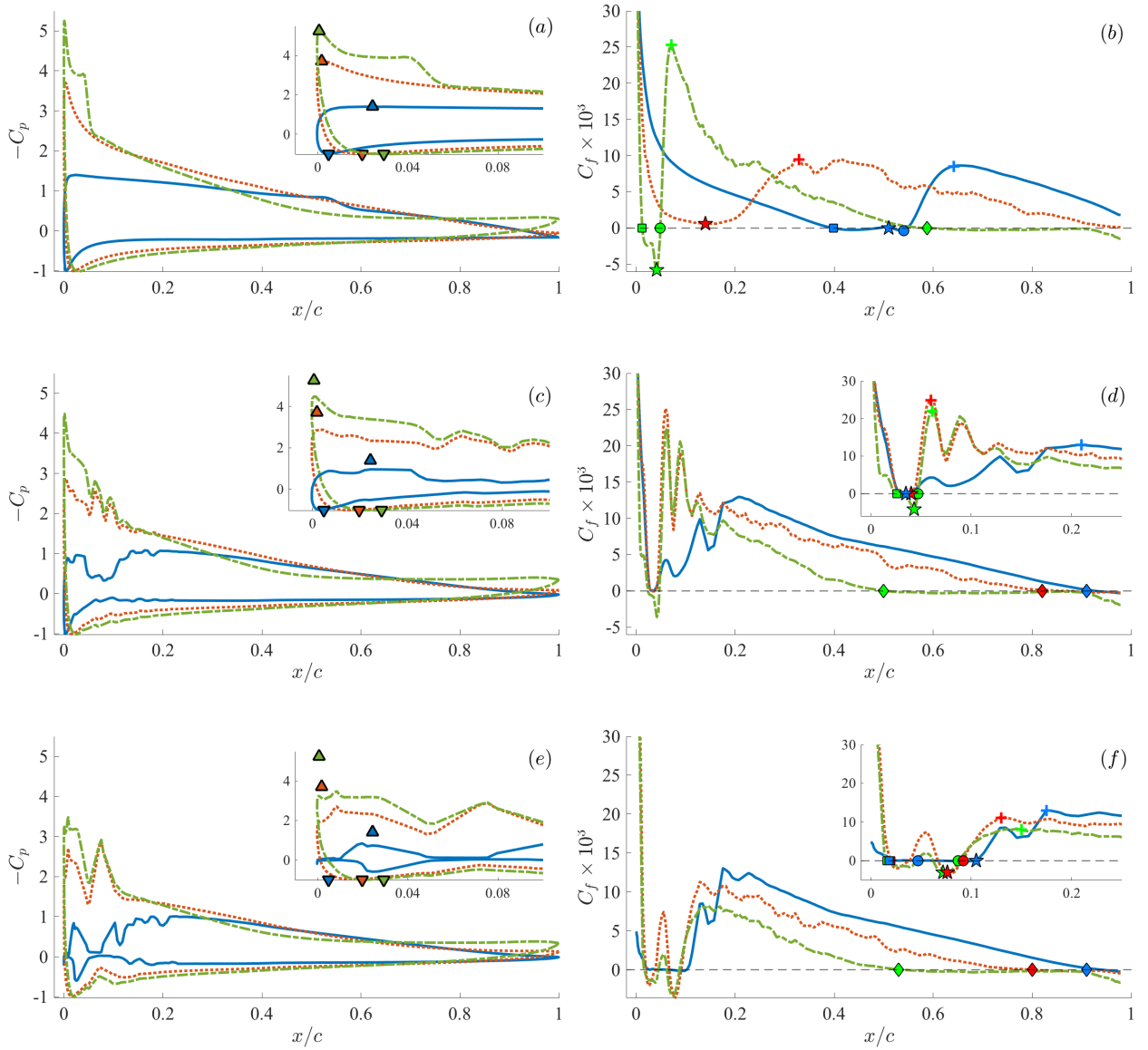
Fig. 6 **Time- and spanwise-averaged** *(a,c,e)* c_p **and** *(b,d,f)* c_f **for:** *(a,b)* **SLE cases;** *(c,d)* **RLE1 cases; and** *(e,f)* **RLE2 cases;** —— $\alpha = 5^o$; ⋯⋯ $\alpha = 10^o$; –·–· $\alpha = 15^o$. **The minimum (△) and maximum (▽) pressure location for the SLE cases are shown on all** c_p **plots for comparison. Laminar separation point** $(x_{sep}; □)$, **transition point** $(x_{tra}; ✦)$; **re-attachment point** $(x_{reat}; ○)$; **transition completion point (+) and trailing edge separation point (◇), wherever applicable, are also indicated in** c_f **plots.**

compared to the baseline smooth cases. The strength of this interaction seems to depend, both, on the roughness geometry and the angle of attack.

Figure 6*(c,d)* show the pressure and friction coefficients for the RLE1 cases. The maximum and minimum pressure of the baseline smooth cases is also shown for comparison in Figure 6*(c)* (inset). We observe that with increasing angle of attack the pressure recovers faster towards the smooth case. The c_p distributions for RLE1-10° and RLE1-15° cases,

in fact, are quite similar to their smooth counterparts (compare with Figure 6*(a)*). This suggests that the effect of the roughness elements becomes less pronounced at higher angles. This observation is also supported by the distribution of friction coefficients for 10° and 15° in the roughness region, which almost overlap each other (Figure 6*(d)*). The effect of roughness on flow transition, thus, depends on the angle of attack. Transition begins at the first row of roughness elements for all three angles of attack. Nevertheless, fully turbulent levels, indicated by the sharp rise with a local maximum in the c_f plot (marked by "+" symbol) is dependent on the angle of attack. While fully turbulent levels are achieved only by the end of roughness zone ($x/c = 22\%$) for the RLE1-5° case, transition in RLE1-10° and RLE1-15° cases is more abrupt (fully turbulent levels around $x/c = 7\%$), akin to the smooth case at 15°. This suggest that although roughness might play an important role in the transition process at lower angles-of-attack, the transition mechanism is governed primarily by the adverse pressure gradient and that the role of roughness may be less significant for higher angles-of-attack.

The surface pressure and skin-friction distribution for the RLE2 geometry, shown in Figure 6*(e,f)*, are substantially different for 5° and 10° cases. At 5°, the roughness causes a quasi-2D separated region in its wake, and the surface pressure in that region has a plateau (see inset of Figure 6*(e)*). As the angle of attack is increased to 10°, only the largest roughness elements play a role (as indicated by the two peaks in Figure 6*(e)*) and the flow skims over the smaller roughness elements very close to the leading edge. The transition mechanisms for 5° and 10° look exceedingly similar, with the fully turbulent levels moving incrementally upstream for the 10° case. The c_p, c_f distribution, coupled with the more streaky-ness of the tangential velocity as discussed in the previous section strongly suggests that the interaction of the incoming flow for the RLE2 case occurs mostly with the top of the elements as the angle of attack is increased, allowing the flow to pass in between the roughness elements and, therefore, showcase increased channelling behaviour. This change in behaviour for the RLE2 case might also be exacerbated by the fact that the roughness size is almost 60% larger than the roughness elements in RLE1 case. At 15° there is marginal change in the c_p and c_f behaviours near the roughness zone, providing further evidence that the variability of the flow in the spanwise direction is substantially reduced beyond the stall angle.

E. Flow channelling

In our previous study we showed that the roughness produces elongated regions of high velocity (called *fast* or *peak* regions) alternating with regions of low velocity (*slow* or *valley* regions). The peak regions were generally aligned with the roughness elements, while the valleys were aligned with the gaps between elements. In the peak regions the velocity profile resembled that of an accelerating boundary-layer, while in the valleys it had strong features of a boundary layer in adverse pressure-gradient. In this section we study this phenomenon further, and discuss how the angle of attack affects it.

Figure 7 shows the time-averaged tangential velocity (U_t/U_o) on a plane parallel to the airfoil surface (at a distance
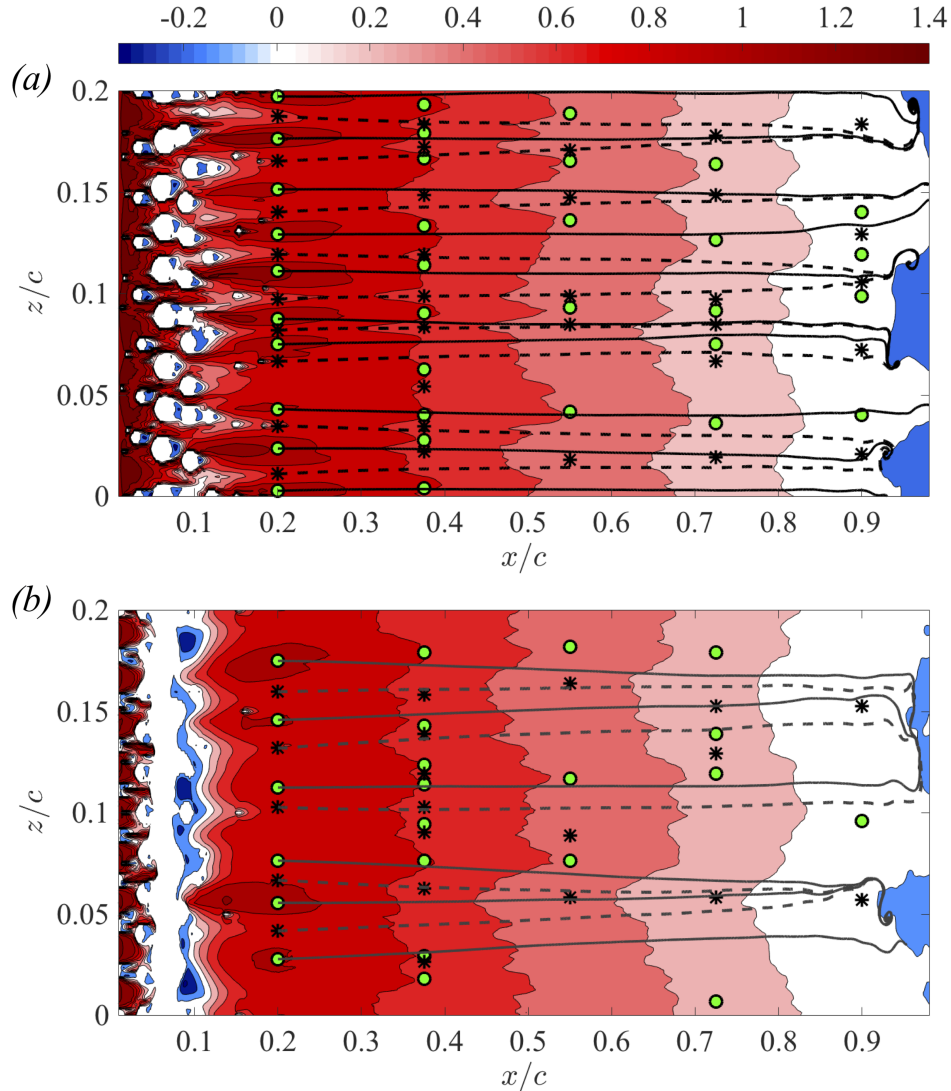
Fig. 7 **Tangential velocity U_t/U_o on a plane parallel to the airfoil surface at a distance, $d/c = 0.002$ from the suction side.** *(a)* **RLE1-5° case;** *(b)* **RLE2-5° case. Fast and slow regions, with a minimum peak-prominence of 20% of maximum tangential velocity at respective streamwise location, are indicated by green circle and black asterisks. The projection on the plane of streamlines originating from the first row of markers are also shown; solid lines: peak regions; dashed line: valley regions.**

$d/c = 0.002$) for the 5° cases. In that figure we also show the prominence of a peak, i.e., the measure of how much a peak stands out from the surrounding baseline of the signal, estimated as the vertical distance between the peak and the lowest contour of the quantity. As previously discussed, we can observe the channels near the leading edge ($x/c \approx 0.2$) in the rough cases. There are alternating regions of fast and slow fluid (highlighted using symbols in Figure 7) originating very close to the last row of roughness elements. While the flow overall slows down downstream of the leading edge, the faster planes near the roughness locations slow down much more rapidly. This is evident in Figure 8, which shows the streamwise evolution of the Rotta-Clauser pressure-gradient parameter (β; [48, 49]) at
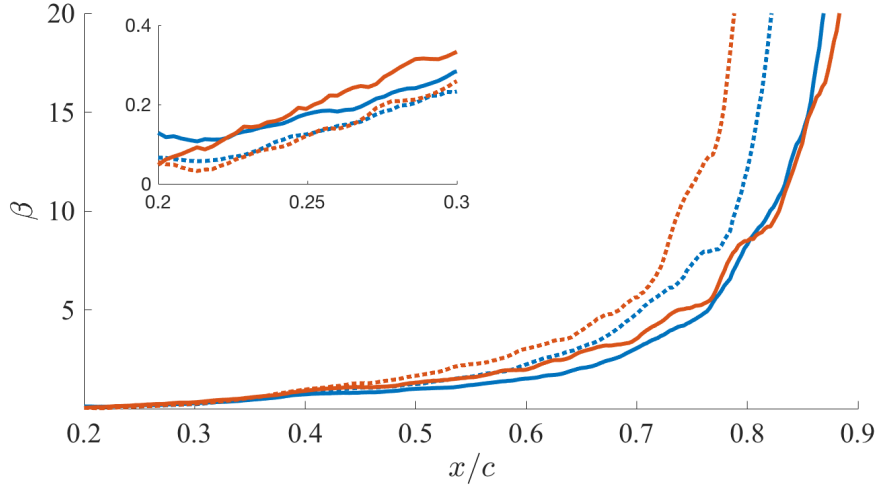
Fig. 8 Evolution of Rotta-Clauser pressure-gradient parameter; blue: RLE1-5° case; red: RLE2-5° case; solid: fast plane; dotted: slow plane. Fast and slow here are identified at $x/c = 0.8$.

spanwise locations representative of fast and slow planes, at $\alpha = 5^o$. β is defined as

$$\beta = \frac{\delta^*}{\langle \overline{\tau}_w \rangle} \frac{dP_e}{dx_t} \tag{7}$$

where δ^* is the boundary-layer displacement thickness and a subscript e denotes the boundary-layer edge. The edge of the boundary layer is identified here, following the work of Griffin *et al.* [50], as the location where the difference between the flow velocity and an "inviscid velocity" obtained using Bernoulli's equation, is 5%. At upstream locations ($x/c < 0.3$, see inset plot in Figure 8), the adverse pressure gradient for a locally fast plane (dotted lines) increases much more rapidly than that for slow planes (solid lines). Mechanisms (to be discussed shortly) related to the interaction of roughness-generated vortices have been found to be the root cause of this flow behaviour. Further downstream this trend continues, such that the local slow regions are in the wake of fast regions from upstream locations and *vice-versa* (Figure 7). Additionally, as the fluid is advected downstream, the adjacent channels merge and the streaks becomes wider and less marked. Nonetheless, significant spanwise variation, particularly in flow separation, is still evident very close to the trailing edge for both the roughness cases.

Lastly, Figure 9 shows the quantity ΔU_t, defined as

$$\Delta U_t(x, d) = \frac{\max\limits_{z}[U_t(x, d, z)] - \min\limits_{z}[U_t(x, d, z)]}{U_e(x)}. \tag{8}$$

ΔU_t quantifies the strength of the channelling as the maximum difference between fast- and slow-moving regions. In line with our prior discussions, we see strong spanwise variations of the tangential velocity over the entire airfoil. At
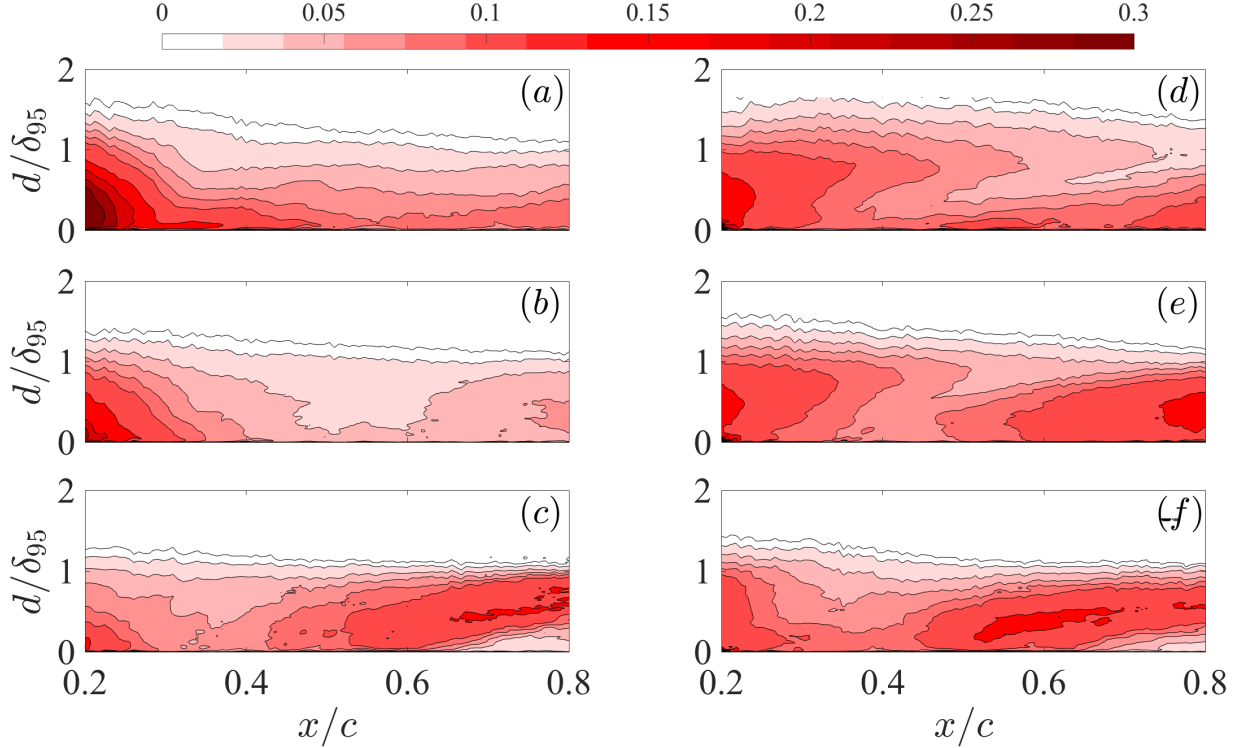
Fig. 9 **Contours of maximum tangential-velocity difference,** (8)**; *(a,b,c)* RLE1 cases *(d,e,f)* RLE2 cases; *(a,d)* 5°; *(b,e)* 10° and *(c,f)* 15°.**

upstream locations these differences extend to the nominally irrotational region above the boundary layer. Although the number of alternating fast- and slow-regions is reduced as the flow moves downstream (that is, with increasing β), the strength of channelling actually increases in the vicinity of the wall ($d/\delta_{95} \lessgtr 0.4$) for lower angles-of-attack. The variation in the effect of α on the two roughness geometries, as seen before for the roughness region, is also quite clear: whereas the strength of channelling decreases for the RLE1 geometry (Figure 9 *(a,b)*), it increases for RLE2 case (Figure 9) *(d,e)*. Further increase in the angle of attack to 15° (Figure 9 *(c,f)*) reduces flow variability within the attached boundary-layer region ($x/c \lessgtr 0.5$) for both the roughness cases. The separated shear layer towards the trailing edge, however, still shows a significant three-dimensional modulation of the flow due to leading edge channelling. The flow retains the memory of its interaction with the leading-edge roughness over the entire airfoil. We also observe that as the magnitude of β increases (towards the trailing edge), the flow variability intensifies for both the roughness types at all angles of attack. With increasing β the spanwise inhomogeneities are amplified; this is analogous to the strengthening of the outer-layer structures caused by an APG in smooth wall boundary layer flows [51, 52], and should be explored further in the future.

Figure 10 shows the instantaneous turbulent structures in the RLE1-5° case visualized by iso-surfaces of the second-invariant of the velocity-gradient tensor Q, defined in(3). Near the leading edge (Figure 10(a)), there are two distinct type of hairpins, based on the underlying mechanism behind their spawning:
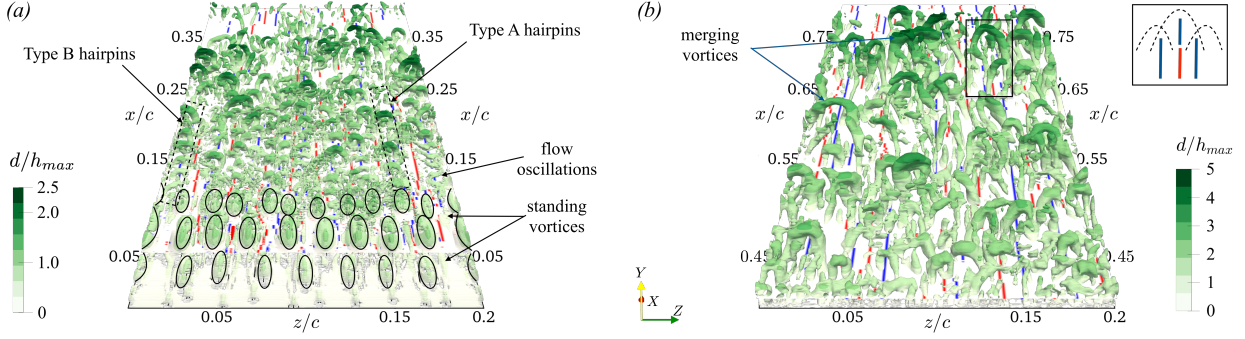
17

Fig. 10 **Iso-surfaces of** Q**-criterion, coloured by distance from the wall,** d **normalized by the maximum roughness height** (h_{max}) **for the RLE1 case.** *(a)* $x/c \in [0, 0.4]$ **and** $Qc^2/U_o^2 = 750$**.** *(b)* $x/c \in [0.4, 0.8]$ **and** $Qc^2/U_o^2 = 150$**. Black ellipses in** *(a)* **show the locations of roughness elements; red and blue lines show the locations of instantaneous fast and slow regions, respectively. The inset in the upper right corner in** *(b)* **shows a schematic of the hairpins arrangement highlighted by a black rectangle in the main plot.**
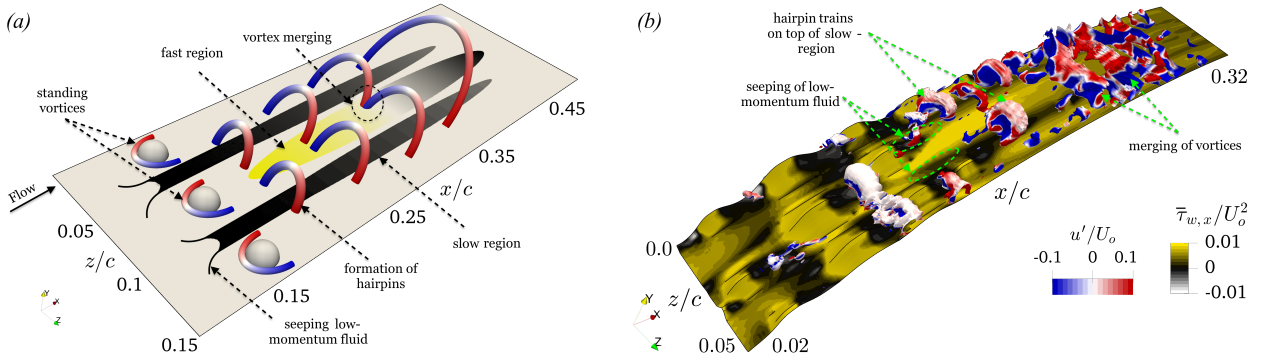

Fig. 11 *(a)* **Schematic representation of the formation of fast and slow regions near the roughness zone. The sketch is not to scale. Blue: negative streamwise vorticity; red: positive streamwise vorticity; yellow: peak regions; black: valley regions;** *(b)* **Iso-surface of pressure fluctuations,** $p' \leq -0.01\rho U_o^2$**, coloured by streamwise velocity fluctuations; the wall shear stress is shown on the airfoil surface.**

- *Type A* hairpin vortices are formed due to shedding associated with the flow over a bluff body, for example in the flow over hemispheres (see Acarlar and Smith [53]).

- *Type B* hairpin vortices are caused by the injection of slow-moving fluid in valley regions. Injection of low-momentum fluid in a laminar boundary layer has been shown by Acarlar and Smith [54] to lead to formation of "oscillations" (also visible in Figure 10*(a)*), associated with the Kelvin-Helmholtz instability, that leads to formation of regular hairpin vortices.

These vortices play a vital role in the dynamics of the peak and valley regions. Figure 11*(a)* and *(b)* show, respectively, a schematic of their development and a visualization of the region near the leading edge (for the RLE1-5° case) where such dynamics can be observed; the vortices are visualized using contours of pressure fluctuations. Low-momentum fluid behind the roughness elements is deviated sideways by the vortices shed by upstream roughness elements, and
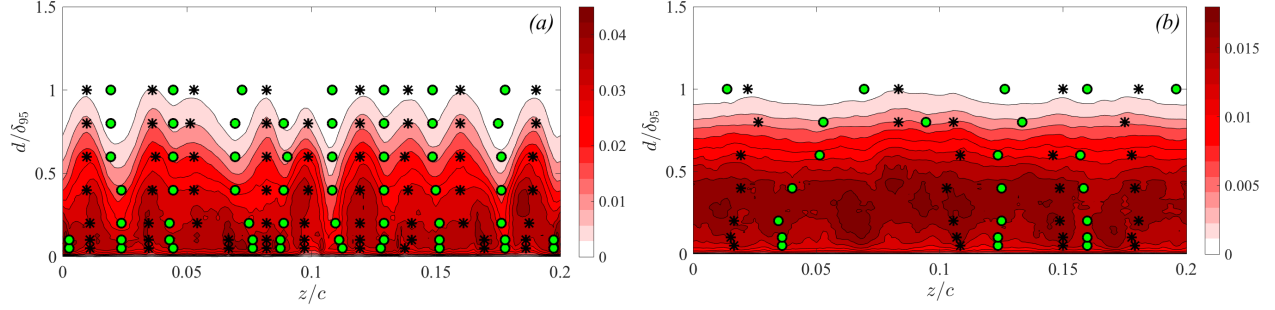
Fig. 12 **Contours of turbulent kinetic energy, $\mathcal{K}/U_o^2$ for RLE1-5° case at two streamwise locations** *(a)* $x/c = 0.2$**;** *(b)* $x/c = 0.8$**. Fast and slow regions, with a minimum peak-prominence (defined in Figure 10) of 20% of maximum tangential velocity at respective wall-normal location, are indicated by green circles and black asterisks.**

becomes trapped in the valley regions, shown by green dashes in 11*(b)*. Injection of this low-momentum fluid spawns Type B hairpin vortices, which are aligned over the valley plane. Two of the valley regions on either side of a roughness element create a channel for the accelerating flow over the roughness element. Further downstream, spanwise merging of these hairpins occurs, highlighted in 11*(b)*; as a result, a bigger hairpin-like structure is formed. The faster-moving fluid in the peak planes slows down, since these planes are positioned between the legs of the new vortex, and merge with the slow-moving fluid in valley regions. Evidence of this merging can be seen in Figure 11*(b)*, at $x/c \approx 0.3$ where both the fast and slow planes from the upstream location have merged together and, consequently, the distribution of wall-shear stress shows minimal variation in spanwise direction.

The interaction between vortices originating near the leading edge causes merging and formation of wider streaks downstream. This is shown in Figure 10*(b)* where bigger, merged vortices are immediately above what will eventually turn into a wider, slower streak. These wider streaks are directly responsible for the three-dimensionality of the separated flow, as they modify the mean flow through the pressure gradient, as seen in the previous section.

Another question that remains to be answered regards the effect of the fast-slow regions on the behaviour of (resolved) turbulent kinetic energy $\mathcal{K} = \overline{u_i' u_i'}/2$, where a prime indicates a fluctuation around the time-averaged value, which is denoted by an overbar. Figure 12 shows the (y, z) distribution of turbulent kinetic energy for the RLE1-5° case at two streamwise locations. Initially (Figure 12*(a)*), the local slow planes show more turbulent activity than the fast plane in the outer region of the boundary layer. This phenomenon, as discussed in our previous work, is due to the entrapment of recirculating fluid in the slow regions, which results in an inflectional velocity profile, which is associated with flow instabilities. Comparison with Figure 10*(a)* shows that the excess TKE in slow planes is associated to Type-B hairpin packets and, hence, is non-stochastic in nature. It is to be noted that near the wall the fast planes have increased TKE levels that can be associated to the higher wall stress. At downstream locations (Figure 12*(b)*), the outer layer still shows more turbulent activity in slow planes, further evidence that the effect of roughness-generated vortices are still present. The dynamics of the inner layer, on the other hand, have a mixed behaviour: there is evidence of both fast and slow

Case	$\alpha = 5^o$			$\alpha = 10^o$			$\alpha = 15^o$		
	x_{sep}^{fp}	x_{sep}^{sp}	x_{sep}^{avg}	x_{sep}^{fp}	x_{sep}^{sp}	x_{sep}^{avg}	x_{sep}^{fp}	x_{sep}^{sp}	x_{sep}^{avg}
SLE	-	-	-	-	-	-	-	-	0.58
RLE1	0.96	0.87	0.93	0.93	0.82	0.86	0.62	0.49	0.51
RLE2	0.95	0.84	0.94	0.95	0.72	0.80	0.67	0.48	0.54

Table 3 **Comparison of trailing-edge-separation location at fast (x_{sep}^{fp}) and slow planes (x_{sep}^{sp}) at different angles of attack. Fast and slow regions were identified in the trailing edge region. The time- and spanwise-averaged separation location (x_{sep}^{avg}) is also listed for comparison. The separation point is defined as the streamwise location where $c_f = 0$.**

planes with increased turbulence levels. While the higher TKE levels for a fast plane is to be expected, the slow plane showing increased fluctuations needs some discussion. As the leading-edge vortices (aligned over the slow planes) advect they cause the spawning, by induction, of new hairpin vortices associated with wall turbulence. One instance of such a phenomenon is shown in Figure 10(b) *(marked by the black box)*. The wall-generated hairpins (smaller in scale; on either side of central roughness generated vortex) are aligned with the legs of the leading edge vortex. Such an alignment would explain the widening and increased turbulent activity at a slow plane.

Figure 13 shows the instantaneous wall-shear distribution for all cases considered for this study. At $\alpha = 5^o$, there is a significant variation in flow separation at different spanwise locations. Although some of these channels lose importance with increase in angle of attack, the separation remains highly three-dimensional even at the highest angle of attack considered. We have quantified the 3D nature of the mean-flow separation in Table 3, which compares the location of the separation point for the local fast and slow regions. The three-dimensionality (as measured by the difference between between x_{sep}^{fp} and x_{sep}^{sp}) increases slightly with angle of attack; for RLE2 this increase is more noticeable, reaching nearly 30% of the chord length.

V. Conclusions

We performed large-eddy simulations of the flow over airfoils with leaading-edge roughness designed to mimic the ice accretions encountered in flight. This study extends the previous work of Kumar *et al.* [4], who considered a NACA 4412 airfoil at $Re = 200,000$ and $\alpha = 5^o$, by investigating the effect of angle of attack on the flow. A case with a smooth leading (SLE) edge was compared with two rough cases of airfoils with leading edge roughness (RLE1 and RLE2). These roughness geometries were representative of difference in ice-accumulation times, with RLE1 representative of initial, primarily 3D accumulation and the RLE2 modelling an accumulation over short time interval, thus yielding a mixed 2D/3D topology. Kumar *et al.* [4] identified spanwise variations of the flow quantities, associated with the three-dimensional topology of the leading-edge roughness elements. They termed this phenomenon "channeling" and described its kinematic characteristics. In this paper we follow up on that work by investigating the dynamical aspect of
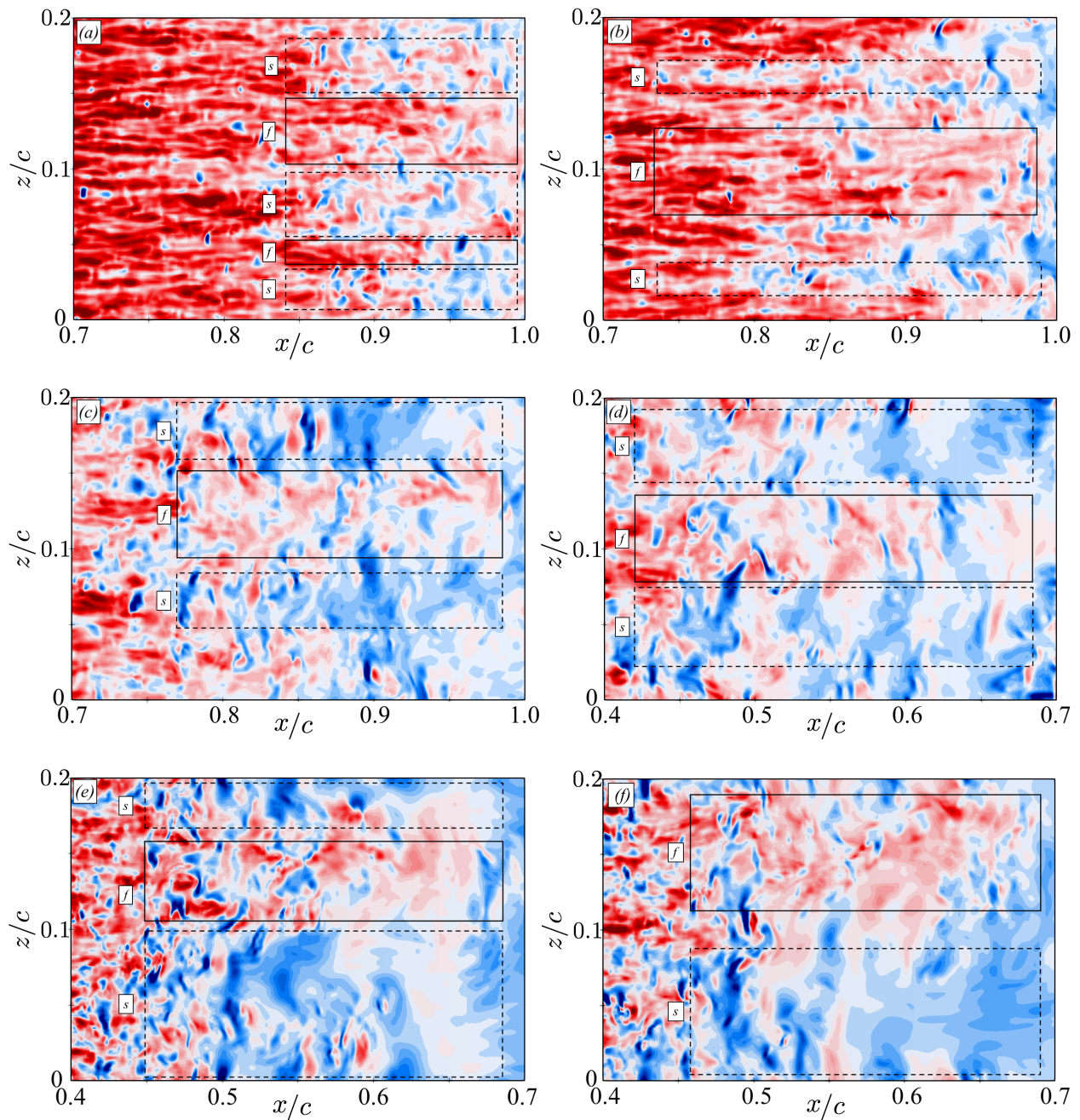
Fig. 13 Contours of the instantaneous wall-shear stress $\tau_w/\rho U_o^2$ near the trailing edge on the suction side of the airfoil. *(a)* RLE1-5° case; *(b)* RLE2-5° case; *(c)* RLE1-10° case; *(d)* RLE2-10° case; *(e)* RLE1-15° case; *(f)* RLE2-15° case. blue: -0.004; white: 0; red: 0.002; slow (*s*) and fast (*f*) moving regions have been marked and labelled.

the phenomenon.

The roughness at the leading edge generates hairpin vortices either through the shedding behind the roughness elements (Type A), or because of the injection of low momentum in the boundary layer (Type B) [53, 54]. The dynamics of fast and slow regions near the leading edge are governed by these hairpins, as fluid in the fast planes slows down as the vortex merge downstream. The merging results in the generation of slow regions, which replace the fast ones in the trailing-edge area, and create a very three-dimensional separation.

We performed simulations at two addition angles of attack, 10° and 15°, on both rough geometries. The interaction of the incoming flow with the roughness elements, and hence the channelling, is found to be strongly dependent on the shape of the roughness. For a primarily 3D geometry, such as the RLE1 case, this interaction and the subsequent flow channelling weakens as the angle of attack is increased. For a mixed 2D/3D topology (RLE2 case), however, increasing the angle of attack forces the flow to interact with the top of the roughness elements only, amplifying the three dimensional behaviour and, consequently, the channelling effect. The effect of leading-edge channelling is visible in three dimensional behaviour of the trailing edge separation, in particular for the RLE2 case, for higher angles of attack.

The findings of this work might have implications for turbulence models applied to iced airfoils. The typical grid spacing used in RANS studies is much larger than typical ice-roughness dimensions, and in most cases the leading edge dynamics cannot be resolved on such grids. The three-dimensionality of the separation, however, has a much larger scale, and reasonable grids should be able to resolve it. However, since it has origin in a much smaller scale, unresolved phenomenon, its root causes cannot be accounted for in turbulence models.

Finally a note on the sensitivity of our results to the specific setup used in this study. First, we employed a very simplified description of the icing geometries themselves. A question that arises, then, is whether the physical aspects of the flow observed and discussed in this work will be relevant to real iced wing or not. Since most of the observed phenomena essentially depend on the fact that the roughness is more or less three-dimensional, the details of the geometry may not be as important. As long as the roughness displays three-dimensional behaviour, most of the observations made here, from the creation of channels to their merging and, finally, their effect on trailing edge separation, will most likely be applicable.

Secondly, we conducted these simulations at a value of Reynolds number that is much lower than flight condition. However, since the size of these channels depends on the roughness dimensions, and not on viscous scales, the problems observed here can be expected to be present at flight Reynolds numbers as well. Available evidence [11–14] of spanwise heterogeneity in fully turbulent rough-wall boundary layers also supports the relevance of the channelling phenomenon discussed here in high Reynolds-numbers problem. The trailing-edge separation-dynamics, however, might be more sensitive to higher turbulence levels in disturbed environments.

Acknowledgments

References

[1] Loftin, L. K., Quest for performance: The evolution of modern aircraft, 468, Scientific and Technical Information Branch, National Aeronautics and Space~..., 1985.

[2] Gent, R. W., Dart, N. P., and Cansdale, J. T., "Aircraft icing," Philosophical Transactions of the Royal Society A: Mathematical, Physical and Engineering Sciences, Vol. 358, No. 1776, 2000, pp. 2873–2911. https://doi.org/10.1098/rsta.2000.0689.

[3] Cebeci, T., and Kafyeke, F., "Aircraft Icing," Annual Review of Fluid Mechanics, Vol. 35, No. 1, 2003, pp. 11–21. https://doi.org/10.1146/annurev.fluid.35.101101.161217.

[4] Kumar, V., Piomelli, U., and Lehmkuhl, O., "Large-eddy simulations of the flow on an aerofoil with leading-edge imperfections," Journal of Turbulence, Vol. 22, No. 11, 2021, pp. 735–760. https://doi.org/10.1080/14685248.2021.1973015, URL https://www.tandfonline.com/doi/full/10.1080/14685248.2021.1973015https://doi.org/10.1080/14685248.2021.1973015.

[5] Lynch, F., and Khodadoust, A., "Effects of ice accretions on aircraft aerodynamics," Progress in Aerospace Sciences, Vol. 37, No. 8, 2001, pp. 669–767. https://doi.org/10.1016/S0376-0421(01)00018-5.

[6] Bragg, M. B., Broeren, A. P., and Blumenthal, L. A., "Iced-airfoil aerodynamics," Progress in Aerospace Sciences, Vol. 41, No. 5, 2005, pp. 323–362. https://doi.org/10.1016/j.paerosci.2005.07.001.

[7] Stebbins, S. J., Loth, E., Broeren, A. P., and Potapczuk, M., "Review of computational methods for aerodynamic analysis of iced lifting surfaces," Progress in Aerospace Sciences, Vol. 111, No. May, 2019, p. 100583. https://doi.org/10.1016/j.paerosci.2019.100583, URL https://doi.org/10.1016/j.paerosci.2019.100583.

[8] Vadlamani, N. R., Tucker, P. G., and Durbin, P., "Distributed Roughness Effects on Transitional and Turbulent Boundary Layers," Flow, Turbulence and Combustion, Vol. 100, No. 3, 2018, pp. 627–649. https://doi.org/10.1007/s10494-017-9864-4, URL http://link.springer.com/10.1007/s10494-017-9864-4.

[9] Ye, Q., Avallone, F., Ragni, D., Choudhari, M., and Casalino, D., "Boundary layer transition induced by distributed roughness array," 11th International Symposium on Turbulence and Shear Flow Phenomena, TSFP 2019, 2019, pp. 19–24. URL http://resolver.tudelft.nl/uuid:fcc3e754-84ef-40a7-8e25-4435c659288f.

[10] von Deyn, L. H., Forooghi, P., Frohnapfel, B., Schlatter, P., Hanifi, A., and Henningson, D. S., "Direct Numerical Simulations of Bypass Transition over Distributed Roughness," AIAA Journal, Vol. 58, No. 2, 2020, pp. 702–711. https://doi.org/10.2514/1.J057765, URL https://arc.aiaa.org/doi/10.2514/1.J057765.

[11] Nugroho, B., Hutchins, N., and Monty, J. P., "Large-scale spanwise periodicity in a turbulent boundary layer induced by highly ordered and directional surface roughness," International Journal of Heat and Fluid Flow, Vol. 41, 2013, pp. 90–102. https://doi.org/10.1016/j.ijheatfluidflow.2013.04.003, URL http://dx.doi.org/10.1016/j.ijheatfluidflow.2013.04.003.

[12] Mejia-Alvarez, R., and Christensen, K. T., "Wall-parallel stereo particle-image velocimetry measurements in the roughness sublayer of turbulent flow overlying highly irregular roughness," Physics of Fluids, Vol. 25, No. 11, 2013, p. 115109. https://doi.org/10.1063/1.4832377, URL http://aip.scitation.org/doi/10.1063/1.4832377.

[13] Barros, J. M., and Christensen, K. T., "Observations of turbulent secondary flows in a rough-wall boundary layer," Journal of Fluid Mechanics, Vol. 748, 2014, p. R1. https://doi.org/10.1017/jfm.2014.218, URL http://journals.cambridge.org/abstract_S0022112014002183.

[14] Willingham, D., Anderson, W., Christensen, K. T., and Barros, J. M., "Turbulent boundary layer flow over transverse aerodynamic roughness transitions: Induced mixing and flow characterization," Physics of Fluids, Vol. 26, No. 2, 2014. https://doi.org/10.1063/1.4864105.

[15] Spalart, P. R., "Strategies for turbulence modelling and simulations," Int. J. Heat Fluid Flow, Vol. 21, 2000, pp. 252–263.

[16] Furbo, E., "Evaluation of RANS turbulence models for flow problems with significant impact of boundary layers," Tech. rep., Uppsala University, 2010.

[17] Durbin, P. A., and Pettersson Reif, B. A., Statistical theory and modeling for turbulent flows, 2nd ed., Wiley, 2011.

[18] Piomelli, U., Rouhi, A., and Geurts, B. J., "A grid-independent length scale for large-eddy simulations," Journal of Fluid Mechanics, Vol. 766, 2015, pp. 499–527. https://doi.org/10.1017/jfm.2015.29.

[19] Rouhi, A., Piomelli, U., and Geurts, B. J., "Dynamic subfilter-scale stress model for large-eddy simulations," Physical Review Fluids, Vol. 1, No. 4, 2016, p. 044401. https://doi.org/10.1103/PhysRevFluids.1.044401, URL https://link.aps.org/doi/10.1103/PhysRevFluids.1.044401.

[20] Nicoud, F., and Ducros, F., "Subgrid-scale stress modelling based on the square of the velocity gradient tensor," Flow, Turbulence and Combustion, 1999, pp. 1–36. https://doi.org/http://sci-hub.tw/10.1023/A:1009995426001.

[21] Lehmkuhl, O., Piomelli, U., and Houzeaux, G., "On the extension of the integral length-scale approximation model to complex geometries," International Journal of Heat and Fluid Flow, Vol. 78, No. May, 2019, p. 108422. https://doi.org/10.1016/j.ijheatfluidflow.2019.108422, URL https://doi.org/10.1016/j.ijheatfluidflow.2019.108422.

[22] Vázquez, M., Houzeaux, G., Koric, S., Artigues, A., Aguado-Sierra, J., Arís, R., Mira, D., Calmet, H., Cucchietti, F., Owen, H., Taha, A., Burness, E. D., Cela, J. M., and Valero, M., "Alya: Multiphysics engineering simulation toward exascale," Journal of Computational Science, Vol. 14, 2016, pp. 15–27. https://doi.org/10.1016/j.jocs.2015.12.007, URL https://linkinghub.elsevier.com/retrieve/pii/S1877750315300521.

[23] Houzeaux, G., Vázquez, M., Aubry, R., and Cela, J. M., "A massively parallel fractional step solver for incompressible flows," Journal of Computational Physics, Vol. 228, No. 17, 2009, pp. 6316–6332. https://doi.org/10.1016/j.jcp.2009.05.019, URL http://dx.doi.org/10.1016/j.jcp.2009.05.019.

[24] Gövert, S., Mira, D., Kok, J., Vázquez, M., and Houzeaux, G., "Turbulent combustion modelling of a confined premixed jet flame including heat loss effects using tabulated chemistry," Applied Energy, Vol. 156, 2015, pp. 804–815. https://doi.org/10.1016/j.apenergy.2015.06.031, URL https://linkinghub.elsevier.com/retrieve/pii/S0306261915007898.

[25] Gövert, S., Mira, D., Zavala-Ake, M., Kok, J., Vázquez, M., and Houzeaux, G., "Heat loss prediction of a confined premixed jet flame using a conjugate heat transfer approach," International Journal of Heat and Mass Transfer, Vol. 107, 2017, pp. 882–894. https://doi.org/10.1016/j.ijheatmasstransfer.2016.10.122, URL https://linkinghub.elsevier.com/retrieve/pii/S0017931016317495.

[26] Rodriguez, I., Borell, R., Lehmkuhl, O., Perez Segarra, C. D., and Olivia, A., "Direct numerical simulation of the flow over a sphere at Re = 3700," Journal of Fluid Mechanics, Vol. 679, 2011, pp. 263–287. https://doi.org/10.1017/jfm.2011.136, URL https://www.cambridge.org/core/product/identifier/S0022112011001364/type/journal_article.

[27] Aljure, D. E., Lehmkuhl, O., Rodríguez, I., and Oliva, A., "Flow and turbulent structures around simplified car models," Computers and Fluids, 2014. https://doi.org/10.1016/j.compfluid.2014.03.013.

[28] Lehmkuhl, O., Lozano-Durán, A., and Rodriguez, I., "Active flow control for external aerodynamics: from micro air vehicles to a full aircraft in stall," Journal of Physics: Conference Series, Vol. 1522, No. 1, 2020, p. 012017. https://doi.org/10.1088/1742-6596/1522/1/012017, URL https://iopscience.iop.org/article/10.1088/1742-6596/1522/1/012017.

[29] Charnyi, S., Heister, T., Olshanskii, M. A., and Rebholz, L. G., "On conservation laws of Navier–Stokes Galerkin discretizations," Journal of Computational Physics, Vol. 337, 2017, pp. 289–308. https://doi.org/10.1016/j.jcp.2017.02.039, URL https://linkinghub.elsevier.com/retrieve/pii/S002199911730133X.

[30] Lehmkuhl, O., Houzeaux, G., Owen, H., Chrysokentis, G., and Rodriguez, I., "A low-dissipation finite element scheme for scale resolving simulations of turbulent flows," Journal of Computational Physics, Vol. 390, 2019, pp. 51–65. https://doi.org/10.1016/j.jcp.2019.04.004, URL https://doi.org/10.1016/j.jcp.2019.04.004.

[31] Trias, F. X., and Lehmkuhl, O., "A Self-Adaptive Strategy for the Time Integration of Navier-Stokes Equations," Numerical Heat Transfer, Part B: Fundamentals, Vol. 60, No. 2, 2011, pp. 116–134. https://doi.org/10.1080/10407790.2011.594398, URL http://www.tandfonline.com/doi/abs/10.1080/10407790.2011.594398.

[32] Löhner, R., Mut, F., Cebral, J. R., Aubry, R., and Houzeaux, G., "Deflated preconditioned conjugate gradient solvers for the pressure-Poisson equation: Extensions and improvements," International Journal for Numerical Methods in Engineering, Vol. 87, No. 1-5, 2011, pp. 2–14. https://doi.org/10.1002/nme.2932, URL https://onlinelibrary.wiley.com/doi/10.1002/nme.2932.

[33] McClain, S. T., Vargas, M. M., and Tsao, J.-C., "Characterization of Ice Roughness Variations in Scaled Glaze Icing Conditions," 8th AIAA Atmospheric and Space Environments Conference, American Institute of Aeronautics and Astronautics, Reston, Virginia, 2016, pp. 1–14. https://doi.org/10.2514/6.2016-3592, URL https://arc.aiaa.org/doi/10.2514/6.2016-3592.

[34] Lehmkuhl, O., Baez, A., Rodríguez, I., and Perez-Segarra, C. D., "Direct numerical simulation and Large-Eddy simulations of the turbulent flow around a NACA-0012 airfoil," 7th International Conference on Computational Heat and Mass Transfer, 2011, pp. 1–8. URL https://upcommons.upc.edu/bitstream/handle/2117/13499/icchmt_NACA0012.pdf%0Ahttp://upcommons.upc.edu/e-prints/handle/2117/13499.

[35] Rosti, M. E., Omidyeganeh, M., and Pinelli, A., "Direct numerical simulation of the flow around an aerofoil in ramp-up motion," Physics of Fluids, Vol. 28, No. 2, 2016, p. 025106. https://doi.org/10.1063/1.4941529, URL http://aip.scitation.org/doi/10.1063/1.4941529.

[36] Zhang, W., and Samtaney, R., "Assessment of spanwise domain size effect on the transitional flow past an airfoil," Computers and Fluids, Vol. 124, 2016, pp. 39–53. https://doi.org/10.1016/j.compfluid.2015.10.008, URL http://dx.doi.org/10.1016/j.compfluid.2015.10.008.

[37] Thomareis, N., and Papadakis, G., "Effect of trailing edge shape on the separated flow characteristics around an airfoil at low Reynolds number: A numerical study," Physics of Fluids, Vol. 29, No. 1, 2017, p. 014101. https://doi.org/10.1063/1.4973811, URL http://dx.doi.org/10.1063/1.4973811http://aip.scitation.org/doi/10.1063/1.4973811.

[38] Almutairi, J. H., Jones, L. E., and Sandham, N. D., "Intermittent Bursting of a Laminar Separation Bubble on an Airfoil," AIAA Journal, Vol. 48, No. 2, 2010, pp. 414–426. https://doi.org/10.2514/1.44298, URL https://arc.aiaa.org/doi/10.2514/1.44298.

[39] Rodríguez, I., Lehmkuhl, O., Borrell, R., and Oliva, A., "Direct numerical simulation of a NACA0012 in full stall," International Journal of Heat and Fluid Flow, Vol. 43, 2013, pp. 194–203. https://doi.org/10.1016/j.ijheatfluidflow.2013.05.002, URL https://linkinghub.elsevier.com/retrieve/pii/S0142727X13000891.

[40] Geuzaine, C., and Remacle, J. F., "Gmsh: A 3-D finite element mesh generator with built-in pre- and post-processing facilities," International Journal for Numerical Methods in Engineering, 2009. https://doi.org/10.1002/nme.2579.

[41] Choi, H., and Moin, P., "Grid-point requirements for large eddy simulation: Chapman's estimates revisited," Physics of Fluids, Vol. 24, No. 1, 2012, p. 011702. https://doi.org/10.1063/1.3676783, URL http://aip.scitation.org/doi/10.1063/1.3676783.

[42] Rodriguez, I., Lehmkuhl, O., Piomelli, U., Chiva, J., Borrell, R., and Oliva, A., "LES-based Study of the Roughness Effects on the Wake of a Circular Cylinder from Subcritical to Transcritical Reynolds Numbers," Flow, Turbulence and Combustion, Vol. 99, No. 3-4, 2017, pp. 729–763. https://doi.org/10.1007/s10494-017-9866-2, URL http://link.springer.com/10.1007/s10494-017-9866-2.

[43] Lehmkuhl, B. O., Park, G. I., Bose, S. T., and Moin, P., "Large-eddy simulation of practical aeronautical flows at stall conditions," Center for Turbulence Research Proceedings of the Summer Program 2018, 2018, pp. 1–10. URL https://web.stanford.edu/group/ctr/Summer/SP18/reports/II_Numerical_Methods/02_Lehmkuhl.pdf.

[44] Lehmkuhl, O., Rodríguez, I., Baez, A., Oliva, A., and Pérez-Segarra, C., "On the large-eddy simulations for the flow around aerodynamic profiles using unstructured grids," Computers & Fluids, Vol. 84, 2013, pp. 176–189. https://doi.org/10.1016/j.compfluid.2013.06.002, URL http://dx.doi.org/10.1016/j.compfluid.2013.06.002https://linkinghub.elsevier.com/retrieve/pii/S0045793013002144.

[45] Mallor, F., "Enabling high-fidelity measurements of turbulent boundary layer flow over wing sections in the MTL wind tunnel," Ph.D. thesis, KTH, Mechanics, 2019.

[46] Ostowari, C., and Naik, D., "Post-stall wind tunnel data for NACA 44XX series airfoil sections," Tech. Rep. 4807, National Renewable Energy Laboratory (NREL), Golden, CO (United States), 1 1985. https://doi.org/10.2172/5791328, URL http://www.osti.gov/energycitations/product.biblio.jsp?osti_id=5791328http://www.osti.gov/servlets/purl/5791328/.

[47] Eljack, E., Soria, J., Elawad, Y., and Ohtake, T., "Simulation and characterization of the laminar separation bubble over a NACA-0012 airfoil as a function of angle of attack," Physical Review Fluids, Vol. 6, No. 3, 2021, p. 034701. https://doi.org/10.1103/PhysRevFluids.6.034701, URL https://link.aps.org/doi/10.1103/PhysRevFluids.6.034701.

[48] Rotta, J., "On the theory of the turbulent boundary layer," Tech. Rep. February 1, 1953, NACA-TM-1344, Washington DC, 1953. URL https://ntrs.nasa.gov/citations/19930093886.

[49] Clauser, F. H., "Turbulent Boundary Layers in Adverse Pressure Gradients," Journal of the Aeronautical Sciences, Vol. 21, No. 2, 1954, pp. 91–108. https://doi.org/10.2514/8.2938, URL https://arc.aiaa.org/doi/10.2514/8.2938.

[50] Griffin, K. P., Fu, L., and Moin, P., "General method for determining the boundary layer thickness in nonequilibrium flows," Physical Review Fluids, Vol. 6, No. 2, 2021, p. 024608. https://doi.org/10.1103/PhysRevFluids.6.024608, URL http://arxiv.org/abs/2010.14656https://doi.org/10.1103/PhysRevFluids.6.024608https://link.aps.org/doi/10.1103/PhysRevFluids.6.024608.

[51] Sanmiguel Vila, C., Vinuesa, R., Discetti, S., Ianiro, A., Schlatter, P., and Örlü, R., "Separating adverse-pressure-gradient and Reynolds-number effects in turbulent boundary layers," Physical Review Fluids, Vol. 5, No. 6, 2020, p. 064609. https://doi.org/10.1103/PhysRevFluids.5.064609, URL https://link.aps.org/doi/10.1103/PhysRevFluids.5.064609.

[52] Tanarro, A., Vinuesa, R., and Schlatter, P., "Effect of adverse pressure gradients on turbulent wing boundary layers," Journal of Fluid Mechanics, Vol. 883, 2020, p. A8. https://doi.org/10.1017/jfm.2019.838, URL https://www.cambridge.org/core/product/identifier/S0022112019008383/type/journal_article.

[53] Acarlar, M. S., and Smith, C. R., "A study of hairpin vortices in a laminar boundary layer. Part 1. Hairpin vortices generated by a hemisphere protuberance," Journal of Fluid Mechanics, Vol. 175, No. -1, 1987, p. 1. https://doi.org/10.1017/S0022112087000272, URL http://www.journals.cambridge.org/abstract_S0022112087000272.

[54] Acarlar, M. S., and Smith, C. R., "A study of hairpin vortices in a laminar boundary layer. Part 2. Hairpin vortices generated by fluid injection," Journal of Fluid Mechanics, Vol. 175, No. -1, 1987, p. 43. https://doi.org/10.1017/S0022112087000284, URL http://www.journals.cambridge.org/abstract_S0022112087000284.